The Astrophysical Journal, 985:145 (14pp), 2025 May 20 https://doi.org/10.3847/1538-4357/adc7ff

Discovery of Small-scale Flows in the Void of a Coronal Mass Ejection with High-cadence Images Acquired by the Metis Coronagraph on Board Solar Orbiter

Alessandro Bemporad[1], Lucia Abbo[1], Kinga Albert[2], Emanuele Amato[1], Vincenzo Andretta[3], Ruggero Biondo[1], Aleksandr Burtovoi[1,4], Daniele Calchetti[2], Vania Da Deppo[5], Yara De Leo[6,7], Silvano Fineschi[1], Federica Frassati[1], Catia Grimani[8,9], Giovanna Jerse[10], Federico Landini[1], Salvatore Mancuso[1], Giampiero Naletto[5,11], Gianalfredo Nicolini[1], Maurizio Pancrazzi[1], Julian Blanco Rodríguez[12], Marco Romoli[4,13], Giuliana Russano[3], Clementina Sasso[3], Daniele Spadaro[6], Marco Stangalini[14], Hanna Strecker[15], David Orozco Suárez[15], Roberto Susino[1], Luca Teriaca[2], Michela Uslenghi[16], and Gherardo Valori[2]

[1] INAF—Osservatorio Astrofisico di Torino, Pino Torinese, Torino, Italy
[2] Max-Planck-Institut für Sonnensystemforschung, Göttingen, Germany
[3] INAF—Osservatorio Astronomico di Capodimonte, Napoli, Italy
[4] Università di Firenze—Dip. Fisica e Astronomia, Firenze, Italy
[5] CNR—Istituto di Fotonica e Nanotecnologie, Padova, Italy
[6] INAF—Osservatorio Astrofisico di Catania, Catania, Italy
[7] Institute of Physics, University of Graz, Graz, Austria
[8] Dip. di Scienze Pure e Applicate, Università di Urbino, Urbino, Italy
[9] INFN, Sezione di Firenze, Italy
[10] INAF—Osservatorio Astronomico di Trieste, Trieste, Italy
[11] Università di Padova—Dip. Fisica e Astronomia “Galileo Galilei”, Padova, Italy
[12] Universitat de València, Catedrático José Beltrán 2, E-46980Paterna-Valencia, Spain
[13] INAF—Osservatorio Astrofisico di Arcetri, Firenze, Italy
[14] Agenzia Spaziale Italiana, Roma, Italy
[15] Instituto de Astrofísica de Andalucía (IAA-CSIC), Apartado deCorreos 3004, E-18080 Granada, Spain
[16] INAF—IASF, Milano, Italy

Received 2025 February 11; revised 2025 March 6; accepted 2025 March 9; published 2025 May 20

Abstract

On 2022 March 26, the ESA Solar Orbiter mission observed the early evolution of a coronal mass ejection (CME). On that day, the spacecraft was at a heliocentric distance of 0.32 au and a longitude separation from Earth of $74^\circ\!.5$. The CME source region, observed with the Solar Orbiter Polarimetric and Helioseismic Imager magnetometer, shows no preexisting filament or flux rope. The event was first observed in the inner corona by the Solar Orbiter Extreme Ultraviolet Imager instrument with the Full Sun Imager telescope, showing the initial propagation of a flux rope seen face-on in the EUV, and formed during the eruption. Higher up, the event was observed by Metis with the Visible Light channel with an unprecedented time cadence of 20 s and a spatial resolution of 20” corresponding to about 4600 km bin^{-1}. The sequence of total brightness images shows the existence of small-scale circular flows inside the expanding flux rope, surrounded by multiple nested arch-shaped features. These motions, never reported so far, occur inside the void of the CME, with projected speed ~40% higher than the CME propagation speed. The formation of the flux rope during the eruption suggests that these motions can be interpreted as a signature of conversion of magnetic writhe into twist, starting from the shearing of a preexisting arcade.

Unified Astronomy Thesaurus concepts: Solar corona (1483); Active solar corona (1988); Coronagraphic imaging (313); Astronomy data analysis (1858); Astronomy image processing (2306); Polarimetry (1278)

Materials only available in the online version of record: animations

1. Introduction

Coronal Mass Ejections (CMEs) are large-scale expulsions of plasma and magnetic field from the Sun’s corona, representing one of the most significant manifestations of solar activity. CMEs are of particular interest due to their potential impact on space weather, as they can interact with Earth’s magnetosphere and cause geomagnetic storms. The study of these explosive events has been greatly advanced through coronagraphic observations, which allow researchers to image the Sun’s corona by blocking the bright light from the solar disk. Over the past few decades, coronagraphs such as the Large Angle and Spectrometric Coronagraph (LASCO) on board the Solar and Heliospheric Observatory (SOHO) and the COR1 and COR2 instruments on board the Solar Terrestrial Relations Observatory (STEREO) have provided invaluable data for understanding the dynamics and morphology of CMEs (G. E. Brueckner et al. 1995; R. A. Howard et al. 2008).

Previous studies based on LASCO and STEREO observations have revealed much about the large-scale structure of CMEs, including their propagation through the heliosphere, their interaction with the solar wind, and their three-dimensional configuration when observed from different vantage points (A. F. R. Thernisien et al. 2006; A. Vourlidas et al. 2013). However, despite significant advances, many questions remain open regarding the fine structure of CMEs, especially at smaller spatial and temporal scales. One of the most intriguing, unsolved issues is the detailed organization of magnetic fields within the body of the CME. Observations have hinted at the presence of filamentary features within CMEs that may trace the underlying magnetic field lines (R. M. E. Illing & A. J. Hundhausen 1986; S. E. Gibson & Y. Fan 2006), but these structures have not been conclusively identified and characterized in most previous data sets due to limitations in temporal and spatial resolution.

The LASCO and STEREO coronagraphs, while instrumental in revolutionizing our understanding of CMEs, typically capture images at cadences ranging from 5 minutes to as much as 45 minutes (P. T. Gallagher et al. 2003; R. C. Colaninno & A. Vourlidas 2009), making it difficult to resolve the rapid dynamic changes that occur during CME evolution, especially in its early phases. Consequently, the detection of finer substructures within CMEs, including the internal filamentary features and their relation to the CME's magnetic field orientation, has been challenging. For instance, studies have suggested the presence of magnetic flux ropes as key components of CME structures (A. Vourlidas et al. 2013), but the precise configuration of magnetic field lines and how they evolve during a CME's propagation are still actively debated (P. F. Chen 2011; C. Jiang et al. 2021).

The existence of multiple filamentary structures in the body of CMEs was noticed a long time ago, in particular, with LASCO observations showing for many events the existence of multiple, concave-outward, bright striations in correspondence to the CME leading edges (e.g., S. P. Plunkett et al. 2000 and references therein) and has been interpreted since the beginning as signatures of the underlying helical magnetic field embedded in the expanding flux rope (e.g., J. Chen et al. 1997; K. P. Dere et al. 1999) and also below the flux rope (e.g., B. E. Wood et al. 1999). Similar features were observed many times after application of wavelet-based methods (G. Stenborg & P. J. Cobelli 2003) to enhance fainter properties. From this kind of image, for instance, multiple nested features in the front of a CME were visible in the LASCO images enhanced with wavelets and presented by J. Lin et al. (2005; see their Figures 4 and 5) and also by S. Mancuso & A. Bemporad (2009; see their Figures 1 and 3). Also, D. I. González-Gómez et al. (2010) noticed in many CMEs the presence of "intertwined magnetic field lines" in the CME core, while "the frontal structure is split into a series of concentric rainbow-like arcades." The possible origin for multiple nested circular features between the front and the core of a CME was first discussed by A. Bemporad et al. (2007), who proposed that (for a specific event observed with the Mauna Loa coronagraph) "magnetic reconnection of field lines wrapped around the rising rope forms the white-light feature observed in between the CME front and the core."

Understanding the origin and evolution of these smaller-scale filamentary features inside the CME bodies could be very important, because these features are usually assumed to be tracers of the underlying magnetic field lines, driving the physical interpretation of observations; nevertheless, these features have never been studied in depth. Interest in this type of structure has now been revived thanks to close-range observations provided by the WISPR heliospheric imager (A. Vourlidas et al. 2016) on board the Parker Solar Probe. Very recently, S. B. Shaik et al. (2024) reported the observations by WISPR of coherent nested rings inside an interplanetary CME, features that have been identified as directly associated with the background helical magnetic field lines in the CME flux rope, by assuming multiple concentric flux surfaces with different twists.

In this context, the recent observations obtained from the Metis coronagraph (E. Antonucci et al. 2020; S. Fineschi et al. 2020) on board the ESA Solar Orbiter mission (D. Müller et al. 2020) and presented here represent a significant advancement. For the first time, a CME has been observed with very high-cadence Visible Light (VL) images, captured every 20 s. This unprecedented temporal resolution provides a unique opportunity to examine the internal structure and evolution of a CME in greater detail, with the potential to resolve the fine-scale filamentary features associated with magnetic field lines. This study presents an analysis of these high-cadence coronagraphic observations, with a focus on identifying and characterizing the fine structures within the CME, contributing to a more detailed understanding of their magnetic configuration. In this paper, after a general description of the event (Section 2) focusing on the Extreme Ultraviolet Imager (EUI; Section 2.1), Polarimetric and Helioseismic Imager (PHI; Section 2.2), and Metis data (Section 2.3), the analysis of the latter data is presented (Section 3), and the results are finally summarized and discussed (Section 4).

2. The March 26 Event

On 2022 March 26, a solar eruption occurred from the northwest limb as seen from the point of view of Solar Orbiter. In particular, on that day, the Solar Orbiter spacecraft was located at a heliocentric distance of 0.3227 au and a Heliocentric Earth EQuatorial (HEEQ) longitude of $75\overset{\circ}{.}50$, while the Parker Solar Probe and STEREO-A spacecraft were at heliocentric distances of 0.6800 au and 0.9668 au and HEEQ of 127.85 and $-33\overset{\circ}{.}327$, respectively (see Figure 1). Since the event was observed at the western limb from Solar Orbiter, and considering its approximate propagation direction projected on the ecliptic plane (blue arrow in Figure 1), none of these spacecraft was expected to detect it with in situ data. However, based on the remote-sensing coronagraphic images, the event was expected to be observed on the plane of the sky of the Metis coronagraph on board Solar Orbiter and to appear as a halo backside event in the coronagraphic images acquired on board the SOHO and STEREO-A spacecraft.

2.1. EUI Observations

The EUI images (P. Rochus et al. 2020) acquired in the Full Sun Imager (FSI) 17.4 nm bandpass (spatial resolution of $4\overset{\prime\prime}{.}44$ pixel^{-1}) showed clearly the early CME evolution, as shown in Figure 2. In particular, the images (EUI data release 6; D. Müller et al. 2017) shown in the top left panel of this figure (19:38:50 UT), acquired with the FSI 17.4 nm bandpass, show a bright and complex loop system extending off-limb in the northwest quadrant (as seen from Solar Orbiter). It is interesting to point out that the preexisting loops appear to be mostly edge-on as seen from Solar Orbiter. The subsequent images acquired with the same filter show the expansion of a circular front (top middle left, 20:08:50 UT), starting to leave the instrument field of view 30 minutes later (top middle right, 20:38:50 UT), and finally disappearing 1 hr later (top right, 21:38:50 UT). The expanding front appears oriented mostly face-on, unlike the preexisting loops. The same evolution is

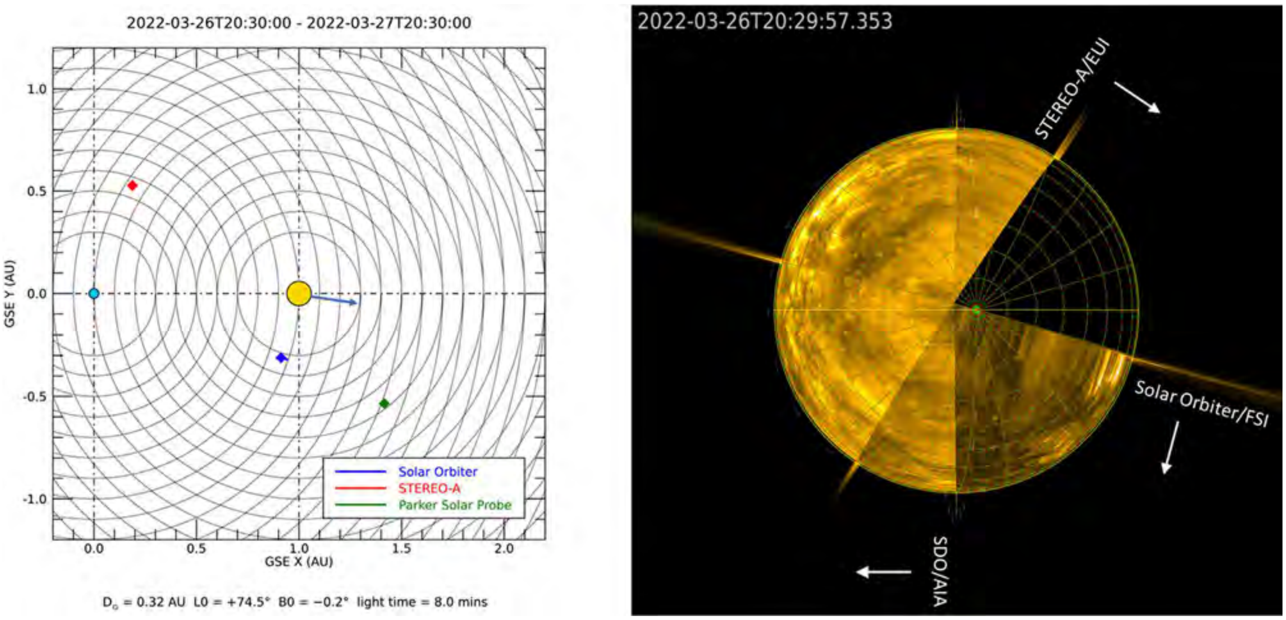

Figure 1. Left panel: locations of different spacecraft (projected on the ecliptic plane) around the time of the event; the blue arrow shows the approximate propagation direction of the event. Dotted circles show distances from the Sun and from the Earth with steps of 0.1 au. Right panel: a combination of EUV images acquired on 2022 March 26, by the EUV telescopes on board Solar Orbiter, STEREO-A, and SDO, as seen from above the solar north pole (grid in Stonyhurst coordinates—image created with J-Helioviewer; D. Müller et al. 2017). The radial features extending over the solar limb correspond to the projected views of the planes of sky as seen from the three different instruments; white arrows show the corresponding locations of the different spacecraft.

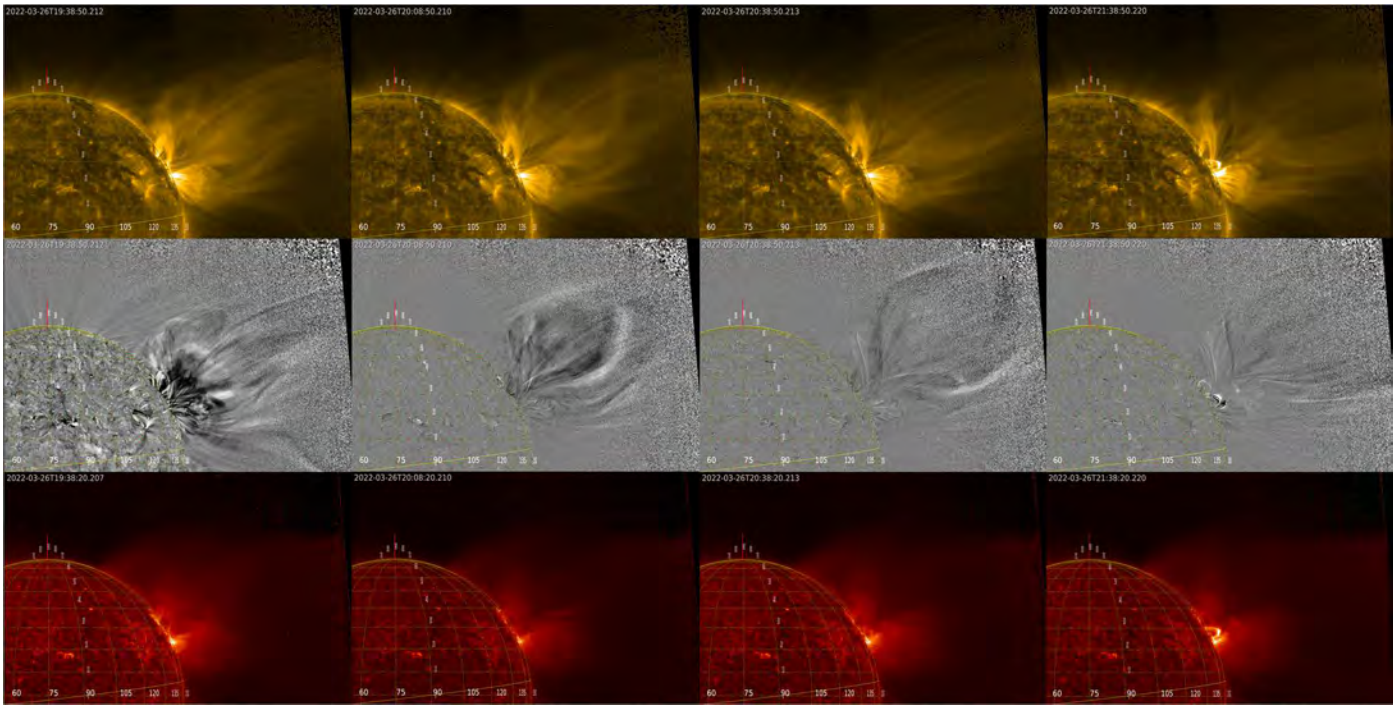

Figure 2. Early evolution of the eruption analyzed in this work as seen by the FSI telescope of the EUI instrument on board Solar Orbiter. Different rows show sequences of images acquired with the 17.4 nm bandpass (top row), the 30.4 nm bandpass (bottom row), and running difference images from the 17.4 nm bandpass (middle row). Different columns refer to images at different times and in particular (from left to right) at 19:38:50 UT, 20:08:50 UT, 20:38:50 UT, and 21:38:50 UT (grid in Stonyhurst coordinates—images created with J-Helioviewer; ?). An animation of the 17.4 nm bandpass sequence is available. The animation begins 2022 March 26 at 14:50:20 and ends the following day at 02:58:20. The real-time duration is 12 s.

(An animation of this figure is available in the online article.)

better outlined with running difference images acquired at the same times and with a cadence of 10 minutes (middle row in Figure 2).

In the meantime, the images acquired by the FSI 30.4 nm bandpass (bottom row in Figure 2) show only the formation of a darker "*V*-shaped" region in the same location of the eruption. Interestingly, the last frames shown in Figure 2 (right column) also show the formation after the eruption of at least two new systems of loop in the source region, which are relatively bright in both filters.

A first standard interpretation of these EUV observations could be as follows: the expanding circular front observed in the 17.4 nm bandpass is a signature of a hollow magnetic flux rope seen mostly edge-on (hence with the axis parallel to the line of sight) and propagating approximately parallel to the plane of sky as seen from Solar Orbiter, hence appearing in the 2D projected images as a circular feature. The flux rope has boundaries with a density lower than the magnetic cavity and is not associated with any visible prominence, as shown by the lack of emission inside the expanding feature in the 30.4 nm bandpass. The appearance of posteruption arcades in both 17.4 and 30.4 nm bandpasses instead is a classical signature of magnetic reconnection in the reconfiguration phases following the eruption.

Nevertheless, the change in orientation between the preexisting loops (seen edge-on over the solar limb) and the expanding circular front (seen face-on) suggests a different interpretation, which will be discussed later. It is also worth noting that the preeruption images do not show evidence of a preexisting cavity in the off-limb coronal loops extending in the source region, suggesting that in this event, the flux rope likely formed during and not before the eruption.

2.2. Photospheric Field Observations

The CME source region NOAA 12965 was classified from the NOAA/USAF Active Region Summary as a $\beta\gamma$ Hale-class active region (AR), corresponding to a complex distribution of sunspots with intermixed polarity. Before the eruption studied here, the magnetograms in the source region showed a predominant larger-scale dipolar magnetic field directed from west to east, with the positive polarity trailing the negative one in the sense of solar rotation. This is evident in the data acquired by Helioseismic and Magnetic Imager (HMI; P. H. Scherrer et al. 2012) on board the Solar Dynamics Observatory (SDO) spacecraft in the days before March 20 (after that date, the AR crossed the solar limb as seen from the Sun–Earth line of sight) and provided at four different selected times in Figure 3. During its transit with the solar rotation, the AR 12965 was the source of three M-class flares on March 14 (M2.0 at 08:29 UT) and March 15 (M1.4 at 12:33 UT and M1.5 at 22:39 UT) and multiple C-class flares. The different data collected in Figure 3 provide interesting information to understand the high level of activity in this AR.

In particular, the first two rows in Figure 3 show (going from left to right) the distribution of sunspots (SDO/HMI continuum images), photospheric fields (SDO/HMI magnetograms), and the overlying systems of loops in the outer (SDO/AIA 17.1 nm bandpass images) and inner (Hinode/X-Ray Telescope (XRT) "Be-Med-Open" images) corona. The first two rows correspond to the time of occurrence of the two M-class flares on March 15 mentioned above, showing that both flares occurred in the AR 12965 at the western side of and below the larger-scale loop system connecting the major opposite polarities from west to east, and in particular corresponding to the smaller-scale negative magnetic polarity embedded inside the larger-scale positive magnetic polarity. This suggests that this was the most active location of region 12965, hence, the site where the magnetic free energy stored in the overlying corona was most likely going to be released leading to flares and/or CMEs also in the subsequent days.

The third and fourth rows in Figure 3 also show that in the subsequent days, this embedded smaller-scale negative polarity evolves, showing new flux emergence and flux cancellation, yet remains persistent and still present when the AR is getting closer to the solar limb as seen from the Sun–Earth line of sight. Nevertheless, when the AR is approaching the solar limb on March 19, the line-of-sight photospheric magnetic field measurements can be affected by projection effects. Moreover, considering the spacecraft locations and the propagation direction of the eruption (Figure 1), AR 12965 was located behind the solar limb as seen from the Earth at the time of the occurrence of the March 26 CME discussed in this study.

Hence, the persistence of this smaller-scale negative polarity in the days before the eruption can be demonstrated only by looking at the magnetograms acquired from a different perspective and in particular, from the data acquired by the PHI instrument (S. K. Solanki et al. 2020) on board Solar Orbiter. Figure 4 shows a detail of this AR with three selected magnetograms acquired by PHI/FDT on March 18 (left panel), March 20 (middle panel), and March 22 (right panel—see the caption for the exact acquisition times).

Due to telemetry limitations, the observations used in this work (Figure 4) were reduced using onboard inversion; only the derived observables (continuum intensity, line-of-sight magnetic field, and line-of-sight velocity—no vector magnetic field measurements for this data set) were downlinked, not the much larger raw data. Unfortunately, due to the limited choice of onboard calibration data at the time, the onboard inversion did not produce the expected results. In particular, visible artifacts resulting from the flats being too small in size, stripes coming from compression errors, and the partial view of the solar disk when the spacecraft was in off-point configuration are evident limitations. Such data are not representative of the PHI/FDT quality and therefore were not released. On the other hand, they are still suitable for the type of morphological analysis presented in this work.[17]

The evolution of magnetograms in AR 12965 provided in Figure 4 clearly demonstrates the persistence of the smaller-scale negative polarity embedded in the larger-scale positive polarity and associated with the strongest M-class flares detected days before. As will be discussed later, this polarity is also the most probable location for the initiation of the CME reported here and in particular for the ejection of the smaller-scale loop system leading to the formation of the CME core and nested inside an overlying larger-scale loop system, leading to the formation of the CME void and front.

2.3. Metis Observations

2.3.1. Description of the Metis Data

On 2022 March 26, the Metis instrument (E. Antonucci et al. 2020; S. Fineschi et al. 2020) acquired images with the VL channel (no images were acquired with the UV detector), with variable cadences, binning, and polarization properties. In particular, the detailed description of the various Metis data sets acquired on 2022 March 26 is summarized in Table 1, which shows that three different acquisition modes were employed: the "Fixed-polarization" (FP), the "tB," and the "pB" modes. In the FP mode, VL polarized intensity images are acquired with a fixed single orientation of the onboard linear polarizer. In the tB mode, the orientation of the polarizer is rotated by 90° (from 0° to 90°) halfway through each acquisition so that one VL

---

[17] Data available on request; please contact sophi_support@mps.mpg.de.

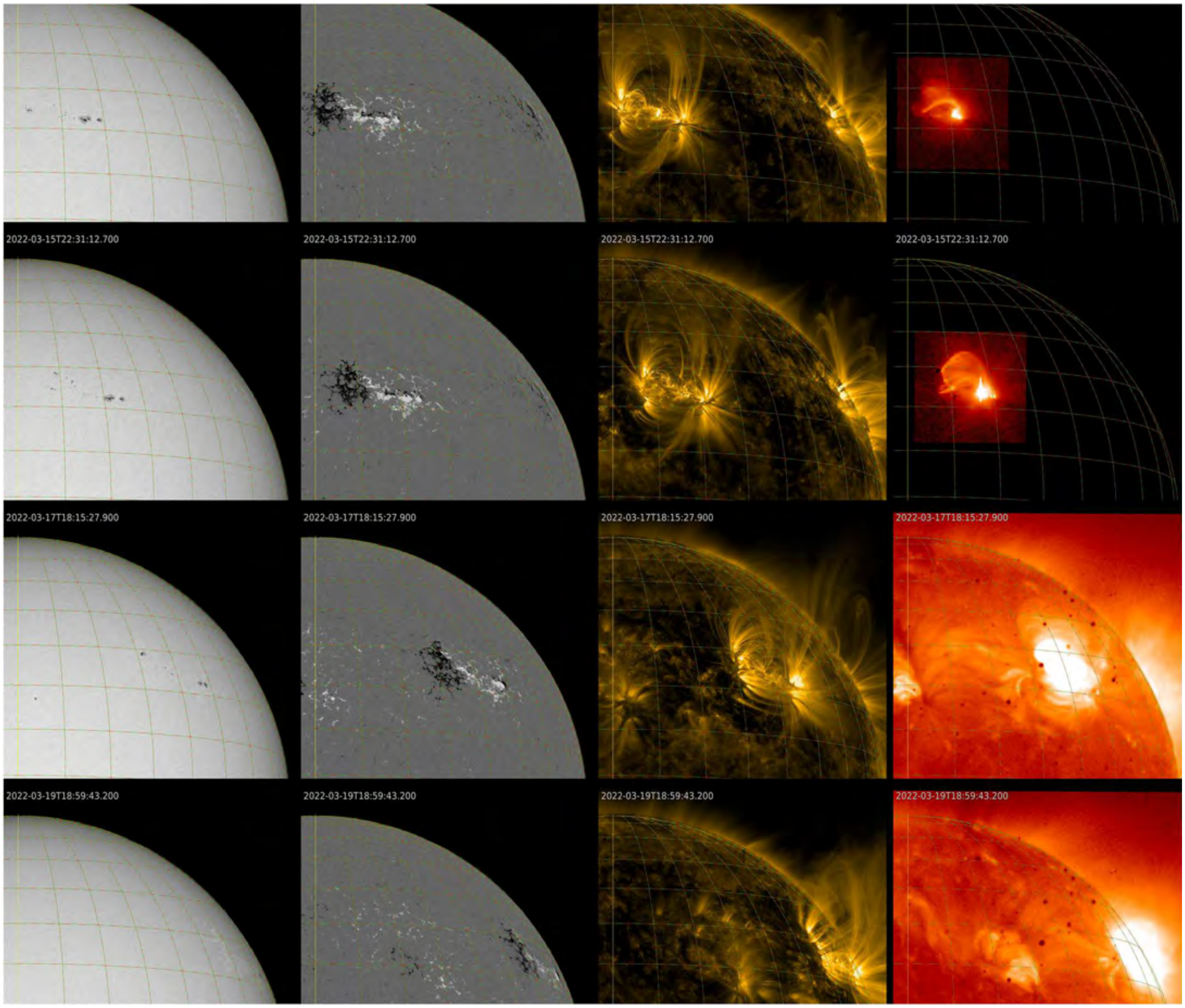

Figure 3. Evolution of the AR 12965 source of the CME studied here. Different columns show data acquired from SDO/HMI in the continuum (leftmost column), SDO/HMI magnetograms (second column), SDO/AIA 17.1 nm bandpass (third column), and Hinode/XRT (rightmost column) with "Be-Med-Open" filter (first two images) and "Open-Al-Mesh" filter (last two images). Different rows refer to different times, in particular, to March 15 at 12:31 UT (top row), March 15 at 22:31 UT (second row), March 17 at 18:15 UT (third row), and March 19 at 18:59 UT (bottom row), as indicated in the top left corner of each panel.

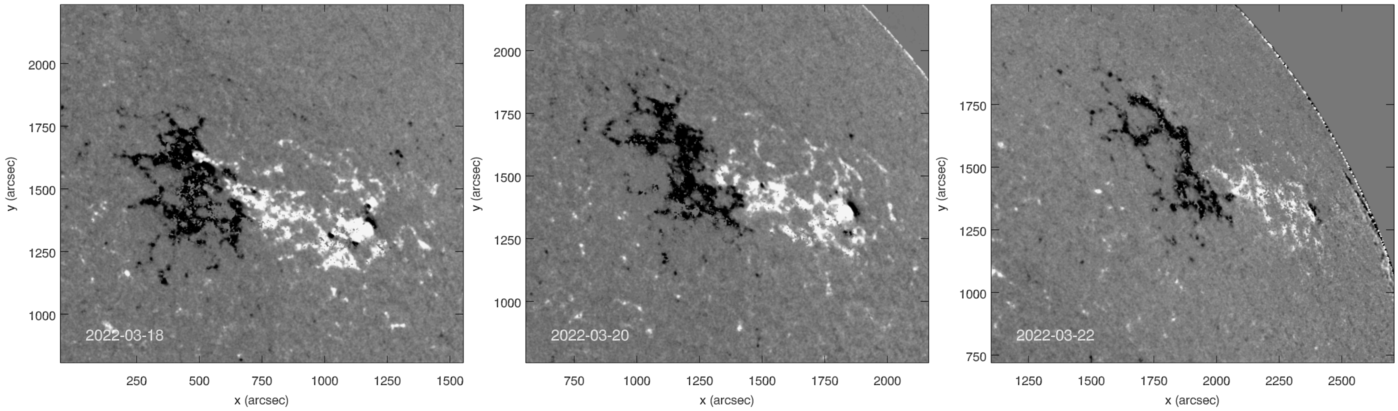

Figure 4. Solar Orbiter magnetograms acquired by PHI/FDT instrument on March 18 20:15 UT (left panel), March 20 at 20:15 UT (middle panel), and March 22 at 21:40 UT (right panel). Each panel provides a zoom over the source AR 12965 oriented to have the solar north up; the plotted magnetic fields are saturated at the value of 100 G.

Table 1

Description of the Main Instrumental Parameters of Metis Data Acquisition on 2022 March 26 (See Section 2.3.1 for Details)

Time Interval (UT)	Observations	Binning	Cadence (s)	DIT (s)	NDIT	DIT × NDIT (s)
00:00–19:40	pB	1 × 1	1200	20	14	280
19:40–20:10	FP	2 × 2	1	1	1	1
20:10–20:50	tB	2 × 2	20	20	1	20
20:50–23:20	pB	2 × 2	1800	30	14	420
23:30–23:59	pB	4 × 4	1220	30	10	300

total-brightness image is directly generated from a single detector integration. In the pB mode, sequences of four polarized intensity images are acquired with four different orientations of the linear polarizer (0°, 45°, 90°, and 135°). The four images of each polarimetric sequence are then combined together on the ground via demodulation by the calibration pipeline to derive both polarized and total-brightness images as well as the angle of linear polarization. For each observation mode, every single image results from the onboard combination of a number of NDIT of images acquired with specific detector integration times (DIT) over a time interval corresponding to the total cadence, resulting in total exposure times DIT × NDIT, as given in Table 1. The VL data were radiometrically calibrated according to Y. De Leo et al. (2023).

Notice that, since images acquired over different time intervals have been averaged on board over different cadences, this implies that images acquired in different time intervals cannot be directly compared to each other, even if the image content is physically of the same quantity. For example, the pB sequence acquired between 20:50 and 23:20 UT (Table 1, fourth row) also provided tB images that could be in principle compared with the tB images supplied by the tB sequence acquired between 20:10 and 20:50 (Table 1, third row) and analyzed here, but the first sequence of tB images was averaged over a cadence of 30 minutes, whereas the second sequence of tB images was averaged over a cadence of 20 s. Hence, dynamic features like the CME studied here are smoothed over very different time intervals in the two sequences, making the relative comparison (e.g., with relative differences) not appropriate. Also, data acquired with different modes (e.g., "Fixed" and "tB") cannot be compared to each other, because each pixel contains different physical information. For these reasons, this work focuses only on the analysis of the tB images acquired with the cadence of 20 s between 20:10 and 20:50 UT on 2022 March 26. Considering the Solar Orbiter heliocentric distance on that day (0.32272 au) and the Metis projected pixel size and spatial binning ($10''.138\ \mathrm{pixel}^{-1}$, binned over $2 \times 2\ \mathrm{pixels\ bin}^{-1}$), the spatial resolution of $20''.276\ \mathrm{bin}^{-1}$ corresponds to 0.00682174 solar radii per bin, or $4745.89\ \mathrm{km\ bin}^{-1}$, and the images have an extension by 1024 × 1024 bins, thus covering a square field of view by 6.985 × 6.985 solar radii.

2.3.2. Description of the CME as Observed by Metis

An example of the Metis field of view on March 26 is shown in Figure 5. In particular, the four panels in this figure show four different running differences obtained by subtracting pairs of tB images separated by a time of 20 minutes. For each panel, the acquisition time of the first frame is provided on the top. Despite the cadence of 20 s, these running differences were constructed using a frame separation time of 20 minutes to be comparable with the classical running differences usually available with the cadence provided by the LASCO coronagraph on board the SOHO mission (G. E. Brueckner et al. 1995); for this reason, we call them "LASCO-like" running differences.

The "LASCO-like" running differences shown in Figure 5 reveal that at the LASCO cadence, the eruption appears in the Metis field of view as a classical "three-part" structured CME, typically consisting of three features: a bright arch-shaped front enclosing a relatively darker cavity and a bright, compact core. These three features are usually associated (see, e.g., T. G. Forbes 2000), respectively, with the coronal plasma pileup (the front) related to the expansion of a magnetic flux rope (the void) often enclosing a denser erupting prominence (the core). The early evolution of this event, as observed by FSI and described above (Figure 2), supports the presence of a propagating magnetic flux rope, but the expanding EUV circular front seems to be closely related to a system of preexisting loops propagating outward, rather than a pileup overlying coronal plasma. Furthermore, no erupting prominence is observed in the EUV, which would typically be associated with the formation of the core. Hence, the application of the classical physical interpretation of the "three-part" structure observed in the "LASCO-like" Metis running differences is more questionable for this event. Despite this peculiarity, in what follows, we keep referring to the different CME parts by using the classical terminology to help the discussion. The proposed interpretation for the formation of this event is discussed in the Section 4 of this work.

This peculiarity is more clearly demonstrated by analyzing the Metis running difference images built by using the real cadence of 20 s for the observations of this event. To better investigate the correspondence between features observed in the EUV by FSI and in the VL by Metis, Figure 6 shows a comparison between two FSI and Metis running differences obtained on March 26 at 20:18 UT (top left panel) and 20:38 UT (top right panel). These images reveal several key aspects. First, the CME appears in the Metis running differences (with a time interval of 20 s between subsequent frames) as composed by multiple nested semicircular features, mostly located in correspondence of the region previously identified in Figure 5 as the CME void. On the other hand, the CME front appears to be made of a larger loop-like feature, corresponding to the expanding EUV loop clearly visible in the images acquired by FSI (see also Figure 2). Also, the CME core appears as a single loop-like feature embedded within the multiple structures observed in the CME void and is only faintly visible in FSI images. Moreover, the footpoints of the larger-scale loop in the front and the smaller-scale loop in the core seem to be anchored in different regions of the solar surface, with the latter rooted slightly northward. This suggests that the loops responsible for the formation of the CME core

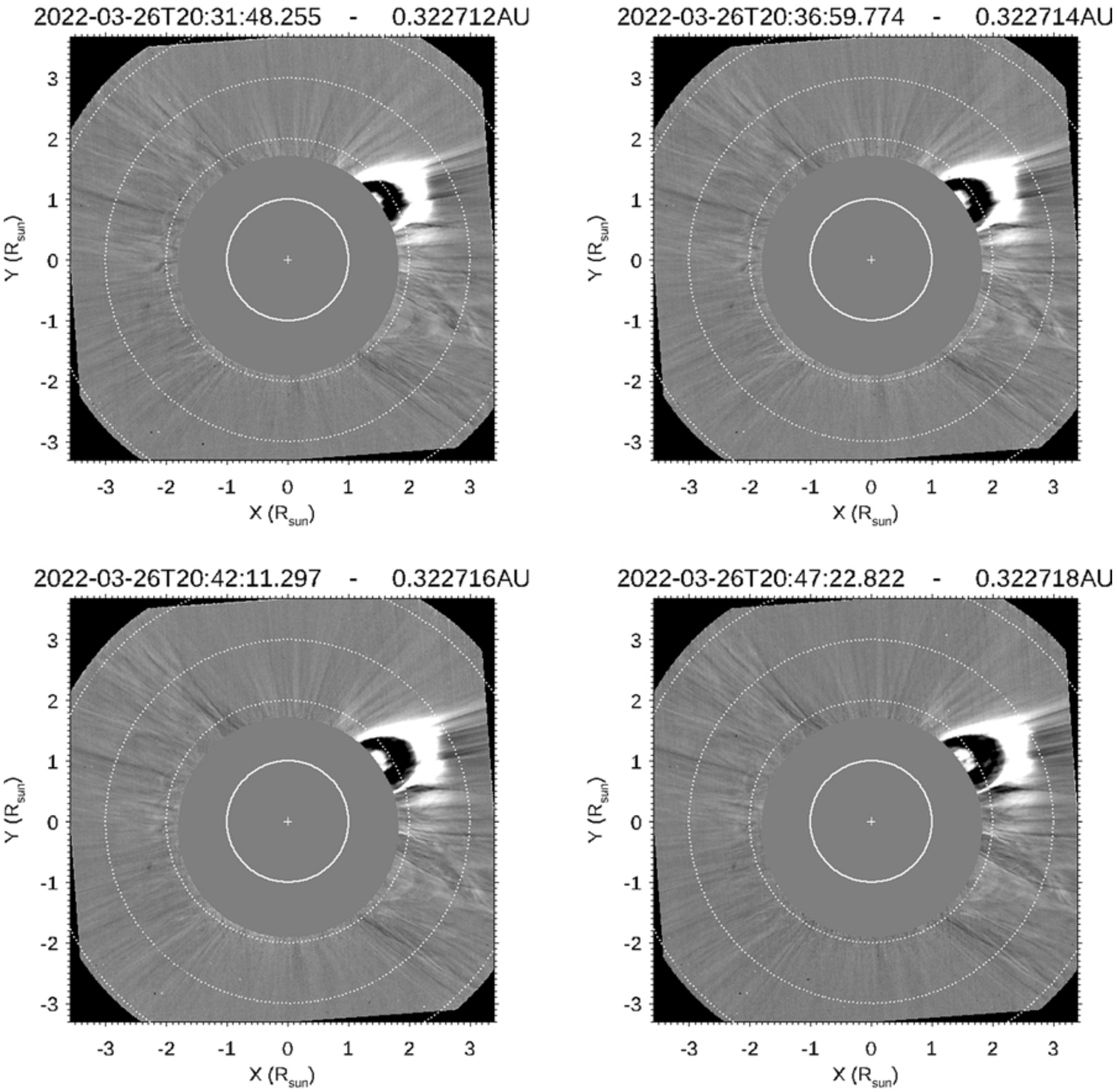

Figure 5. Example of Metis running differences obtained from tB images acquired with a cadence by 20 s, but by subtracting images separated by a time difference of 20 minutes, in order to reconstruct examples of "LASCO-like" running differences. For each difference image, the time indicated on the top corresponds to the acquisition of the first one. The solid white circle provides the projected size of the Sun behind the instrument occulter, while dotted circles provide reference projected distances of 2, 3, and 4 solar radii. The animation runs from 20:31:27 to 20:51:53 on 2022 March 26. The real-time duration is 3 s.

(An animation of this figure is available in the online article.)

and void are bridging over different regions of the photospheric polarity inversion line on the solar surface.

2.3.3. Interpretation of Metis Observations

To help the visualization of these distinct features, the bottom panels of Figure 6 show the corresponding locations of the expanding CME core (solid red line), CME front (solid blue line), and CME void (yellow solid line), along with the nested semicircular structures visible inside the void. These two representations were drawn matching the features visible in the running difference images in the top panels, respectively, at 20:18 UT (bottom left) and 20:38 UT (bottom right). Notice also the superposition along the line of sight of the two footpoints connected with the expanding CME void, a possible signature of a twisting motion of the expanding loop arcades. In line with the evolution shown by FSI images and the corresponding schematic representations, the observed features could be interpreted as an expanding flux rope (outlined with a yellow solid line in the bottom panels of Figure 6) with its axis nearly parallel to the line of sight, enclosing multiple nested layers, that become visible due to density gradients associated with the helical structure of the background magnetic fields. Nevertheless, a more careful inspection of the observations suggests a slightly different interpretation. Specifically, the panels in Figure 6 also show that the loops associated with the flux rope (hence the CME void) and those associated with the CME core are not anchored with their footpoints in the same location of the solar surface. Instead, the loop associated with the CME core is rooted northward with respect to the footpoints of the loop enclosing the CME void. This implies that the CME was likely formed by the destabilization of a smaller-scale loop system interacting with a nearby and overlying larger-scale loop system, leading to its expansion. Considering that (as discussed above) the most active location in the source AR 12965 corresponds to the smaller-scale

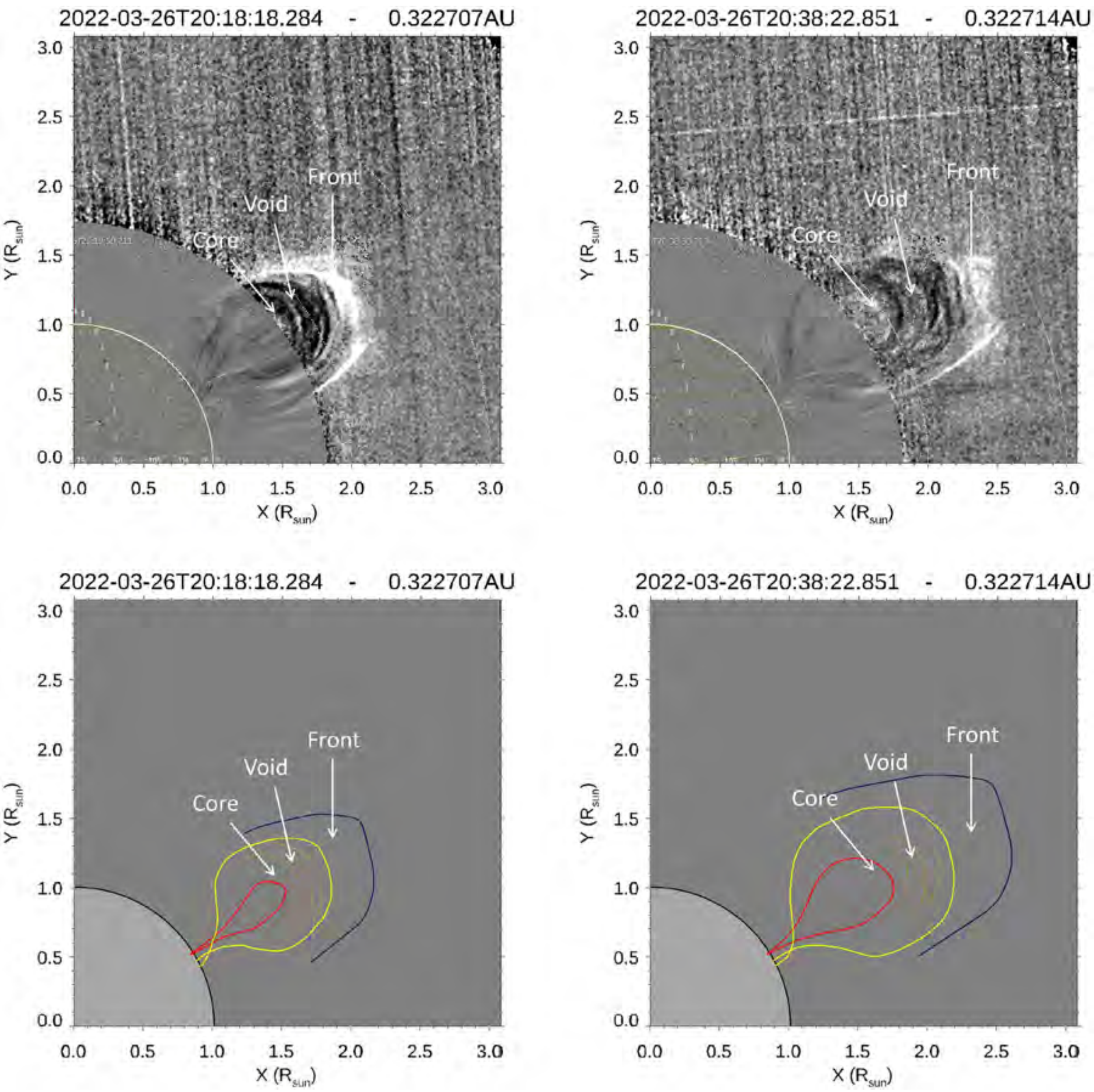

Figure 6. Top: comparison between two FSI running differences (time interval 10 minutes) and the corresponding Metis running differences (time interval 20 s). Bottom: tentative identification in the same difference images of the locations of main CME parts (core—red; void—yellow; front—blue).

negative polarity embedded within the larger-scale westward positive polarity, it is likely that the smaller-scale loop system (solid red lines in the bottom panels of Figure 6) was destabilized there, leading to the formation of the CME core. Its expansion destabilized the overlying larger-scale loop system connecting the west-to-east major opposite polarities of AR 12965, leading to the formation of the CME void and flux rope. Finally, the expansion of the flux rope led to the pileup of the overlying coronal plasma, creating a denser region observed as the CME front. All these considerations will be framed in a single scenario that will be discussed in the last paragraph of this work.

3. Metis Data Analysis

In order to study in detail the evolution of the expanding CME using high-cadence (20 s) data, a sequence of successive running difference frames was assembled into a single animation. To increase the visibility of the fainter features and to normalize each difference image to the average value by minimizing the possible fluctuations in the total intensity, each difference frame was divided by the average of the two frames used in the subtraction. An example of nine consecutive difference images covering almost the whole interval of high-cadence observations is provided in Figure 7 (an animation built with all the available images is also provided). This sequence (focusing only over the northwest quadrant where the CME propagated) shows that between 20:10 and 20:50 UT, Metis observed the early propagation of the CME with the front reaching a projected heliocentric distance of about 2.9 solar radii at the end of the sequence when also the CME void and core become much fainter and almost no longer distinguishable.

A careful visual inspection of the full sequence of running differences (available in the accompanying animation) allowed us to discover a very interesting phenomenon. Not only does the CME void exhibit a nested structure with at least three concentric semicircular loops embedded between the CME front and the core (as outlined in the bottom panels of Figure 6, but these nested features show the existence of density

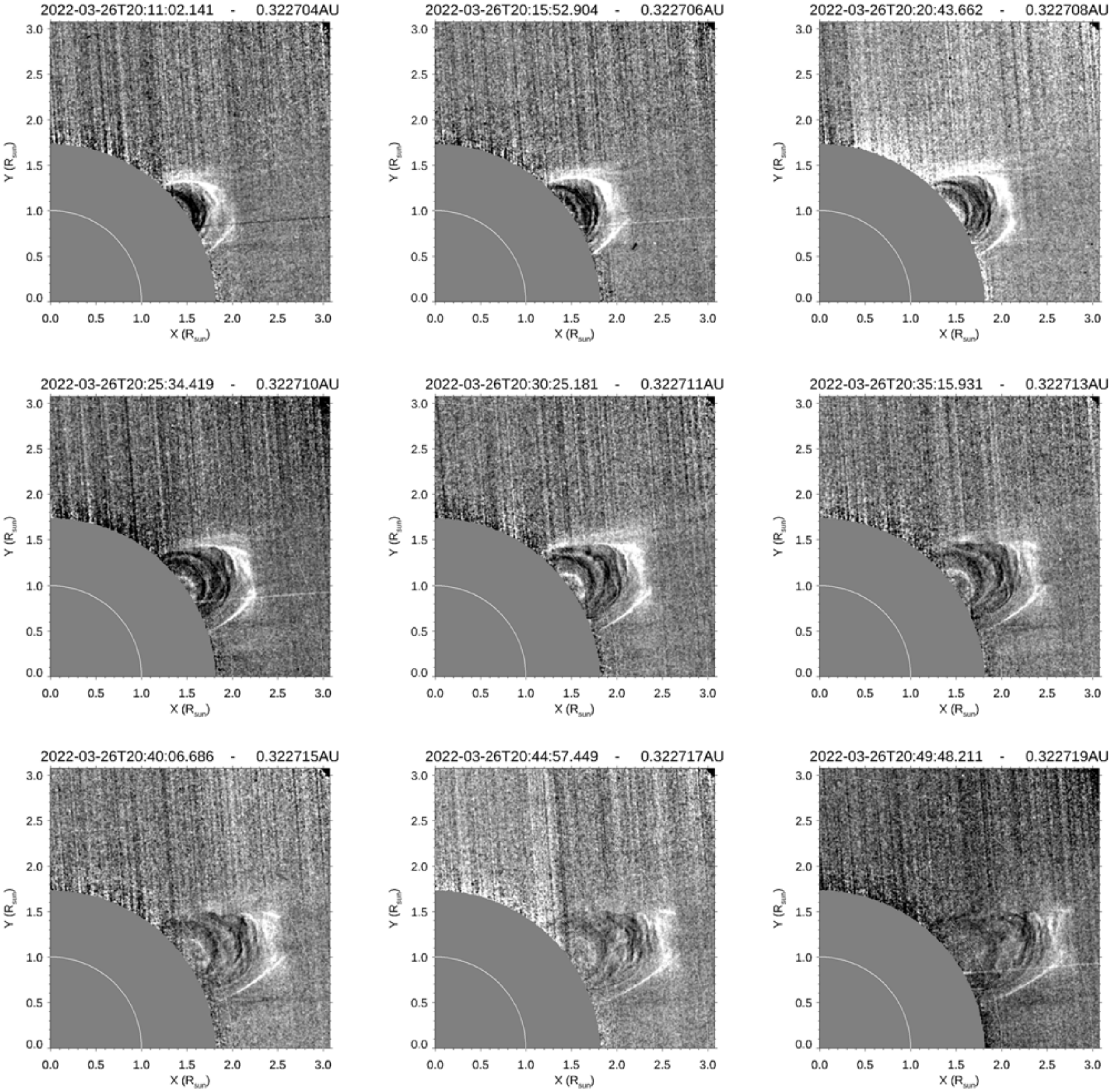

Figure 7. Sequence of running differences (northwest quadrant) built with the high-cadence (20 s) Metis images acquired on 2022 March 26. This figure covers in nine panels almost the whole observation interval going from 20:10 to 20:50 UT with steps of 14 frames corresponding to a time interval of 280 s, plus a small delay by ∼0.6 s between the end of acquisition of the previous image and the beginning of acquisition of the next image. In each panel, the bottom left gray circular region corresponds to the occulted area, while the white arc of circumference represents the solar disk. The animation runs from 20:10:41 to 20:51:32 on 2022 March 26. The real-time duration is 5 s.

(An animation of this figure is available in the online article.)

inhomogeneities following the nested features and moving clockwise during the CME propagation (see also Figure 8 for a better view of such inhomogeneities). To our knowledge, such plasma motion inside the void of a CME has never been reported so far.

In order to properly characterize these motions, the sequence of running differences has been analyzed as follows. First, to determine the radial propagation speed of different CME parts, the standard time-distance map (also called "J-maps") has been built, by cutting out radial intensity profiles extracted at a fixed latitude over a sequence of images. The time-distance map was built by extracting radial profiles from the running difference images at a fixed latitude of 30° north (chosen as the CME void propagation latitude), as illustrated by the blue dashed lines in the four panels of Figure 8. The resulting map is given in Figure 9 after a subtraction (to enhance fainter features) of the radial intensity profile averaged over all the acquired images. This figure also provides in the bottom left corner five reference lines showing the expected slopes corresponding to different velocities ranging from 100 to 300 km s^{-1}. The outer and broader propagating bright feature can be easily identified as the CME front, while the lower darker feature can be associated with the CME void, followed by the slower-moving CME core.

Within the first 25–30 minutes of observations, the features appear to propagate with negligible acceleration, exhibiting different velocities depending on the specific features of about

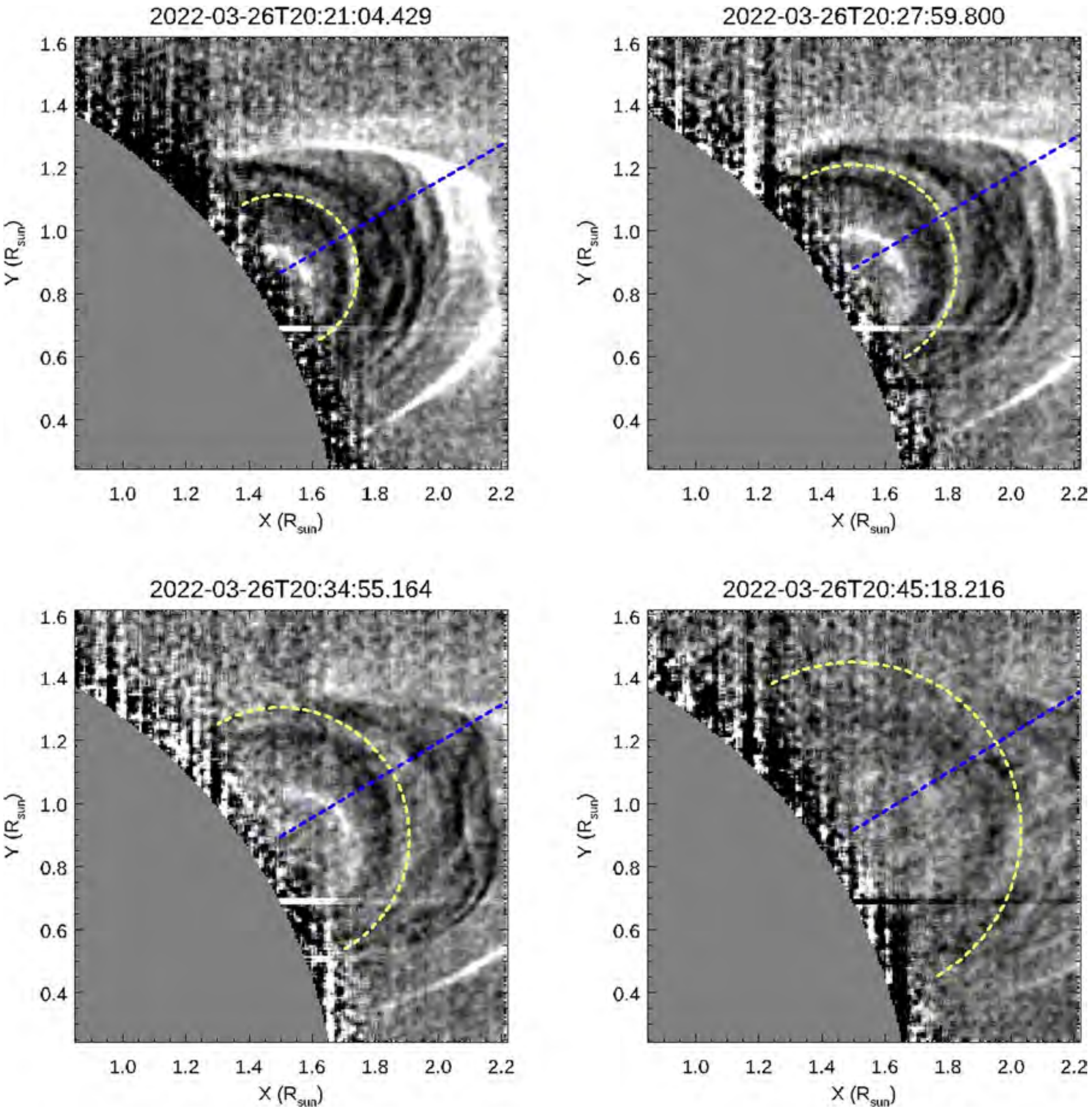

2022-03-26T20:21:04.429

2022-03-26T20:27:59.800

2022-03-26T20:34:55.164

2022-03-26T20:45:18.216

Figure 8. Locations of the vertical (dashed blue lines) and circular (dashed circle lines) strips employed to build, respectively, the time-altitude map of the CME and the time-angle map inside the flux rope.

$(190 \pm 15)\,\mathrm{km\,s^{-1}}$ for the CME front, $(140 \pm 10)\,\mathrm{km\,s^{-1}}$ for the CME void, and $(90 \pm 15)\,\mathrm{km\,s^{-1}}$ for the CME core (as determined with linear fitting of tracks). These velocities are projected onto the plane of the sky but close to the real unprojected values, considering that the CME source region was located at the solar limb as seen from Solar Orbiter. The tracking of different features is no longer possible above 2.5 solar radii, because the tracks become too faint. Nevertheless, Figure 9 suggests that approximately 25–30 minutes after the beginning of the observations at 20:10 UT, some tracks have a clear deceleration trend, indicating a decrease in the propagation velocity.

Given the above radial velocities, it was also possible to define a circular coordinate, running clockwise along a semicircle, whose center and radius have been optimized to track one of three structures nested within the CME void. The locations of these coordinates are shown in Figure 8 at four different times, represented by the semicircular yellow dashed line. After rescaling each semicircular track to its true length in solar radii, the resulting map is provided in Figure 10, along with five reference lines (similar to those provided in Figure 9) showing the expected slopes for assumed velocities ranging from 100 to $300\,\mathrm{km\,s^{-1}}$. This map shows the presence of multiple motions occurring within the expanding CME void, with some tracks exhibiting linear velocities of about $(200 \pm 15)\,\mathrm{km\,s^{-1}}$.

An interesting result is that these circular motions have velocities (also projected onto the plane of the sky) ~40% higher than the radial propagation velocity of the CME void where they have been observed. Moreover, some tracks in Figure 10 clearly show toward the end of the observation period (starting 35 minutes after 20:10 UT) a gradual decrease in velocity, eventually reaching values comparable to the radial propagation velocity of the void. As mentioned above, a similar deceleration trend is observed in the radial propagation velocities. From a theoretical perspective, this suggests two possible interpretations: (1) a cause–effect connection between the larger-scale motion of the CME and the smaller-scale

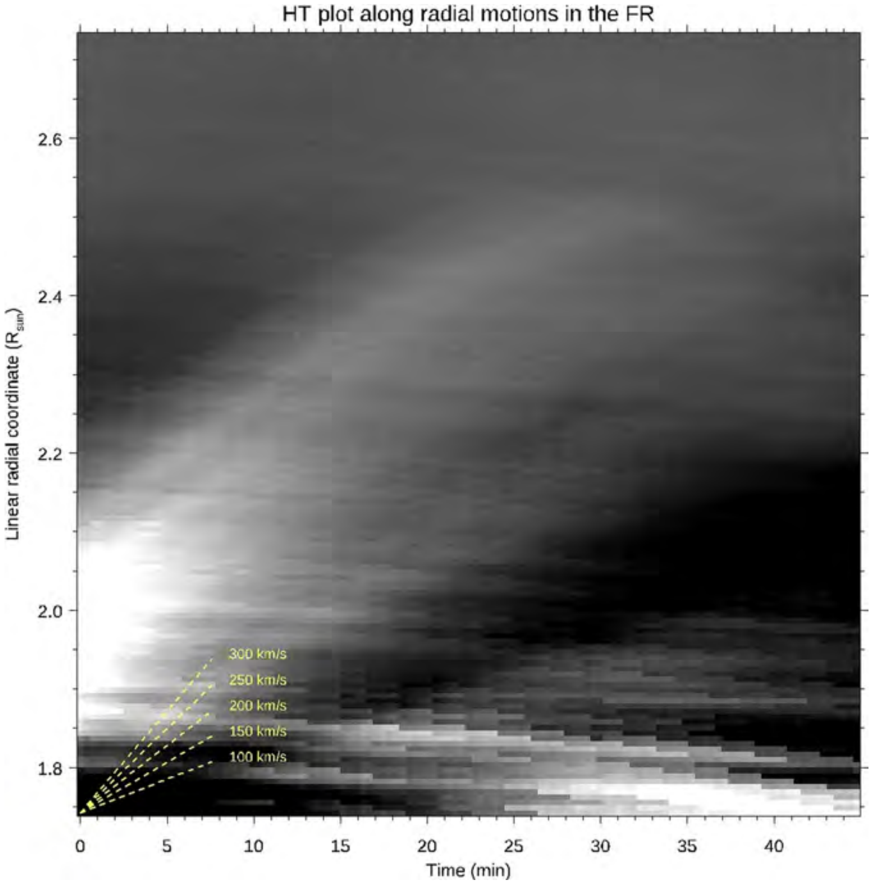

Figure 9. Time-distance map resulting by cutting radial intensity profiles from the running difference images at constant latitude of 30°. The bottom left dashed lines show the reference inclinations of tracks for different theoretical speeds between 100 and 300 km s^{-1}.

motions observed inside the erupting void or (2) a common physical origin for both motions. These interpretations are discussed in Section 4.

4. Discussion and Conclusions

On 2022 March 26, a CME was observed by the instruments on board the ESA Solar Orbiter spacecraft, particularly by the FSI and Metis instruments, while PHI observed the photospheric magnetic fields in the CME source region. Metis observed the early propagation of the CME for over 40 minutes in the VL channel, with an unprecedented time cadence of 20 s. These observations showed not only the existence of multiple nested semicircular features within the CME void but also the occurrence of circular flows inside the void. Surprisingly, these flows have projected speeds ∼40% greater than the propagation speed of the CME void in which they are observed. The kinematic of these flows is similar to that of the whole CME, showing an initial constant speed followed by deceleration. Moreover, the observed CME was not associated with any preexisting filament or coronal cavity in the EUV, suggesting that for this event, the formation of the magnetic flux rope occurred during and not before the eruption. Besides that, the combined Metis and FSI running difference images show that the CME core and void were anchored at different latitudes at the solar surface. All these pieces of information make the theoretical interpretation of these motions more complicated for the reasons discussed below.

Helical flows are a distinct observational feature of CMEs that arise from the underlying twisted magnetic structures of the ejected plasma. Such flows have been identified in both coronagraphic and EUV images, providing critical evidence for the flux-rope topology of many CMEs. Coronagraphic observations often reveal large-scale structures with spiral or helical patterns in the expanding CMEs, especially in three-part CMEs (see, e.g., J. Krall et al. 2001; A. Vourlidas et al. 2013). EUV imaging observations often show clear evidence of filament rotation and/or untwisting during the early stages of CME eruption, in agreement with the theoretical idea of an instability associated with kink instability (T. Török & B. Kliem 2005) and activated once the total twist of a helical flux tube exceeds a limit value (see, e.g., D. R. Williams et al. 2005; P. Kumar et al. 2012; Y. Zhou et al. 2023). These observations were complemented by Doppler measurements of line-of-sight flows that confirm rotational or helical plasma motions along magnetic field lines during the eruption phases (e.g., E. Antonucci et al. 1997; A. Ciaravella et al. 2000; A. C. Sterling et al. 2012). Helical deformation during the instability is a direct consequence of the intrinsic twist of a flux rope, which is converted into helical motion as the rope expands and erupts.

Nevertheless, in the case of the March 26 event, no preexisting filament, filament channel, or coronal cavity was detected prior to the eruption. Consequently, the observed circular plasma flows cannot be interpreted in the light of the classical kink-instability model, as untwisting motions occurring inside a kink-unstable flux rope. If the expanding circular front observed by FSI in EUV (Figure 2) and the three-part structure observed by Metis in VL (Figure 5) were associated

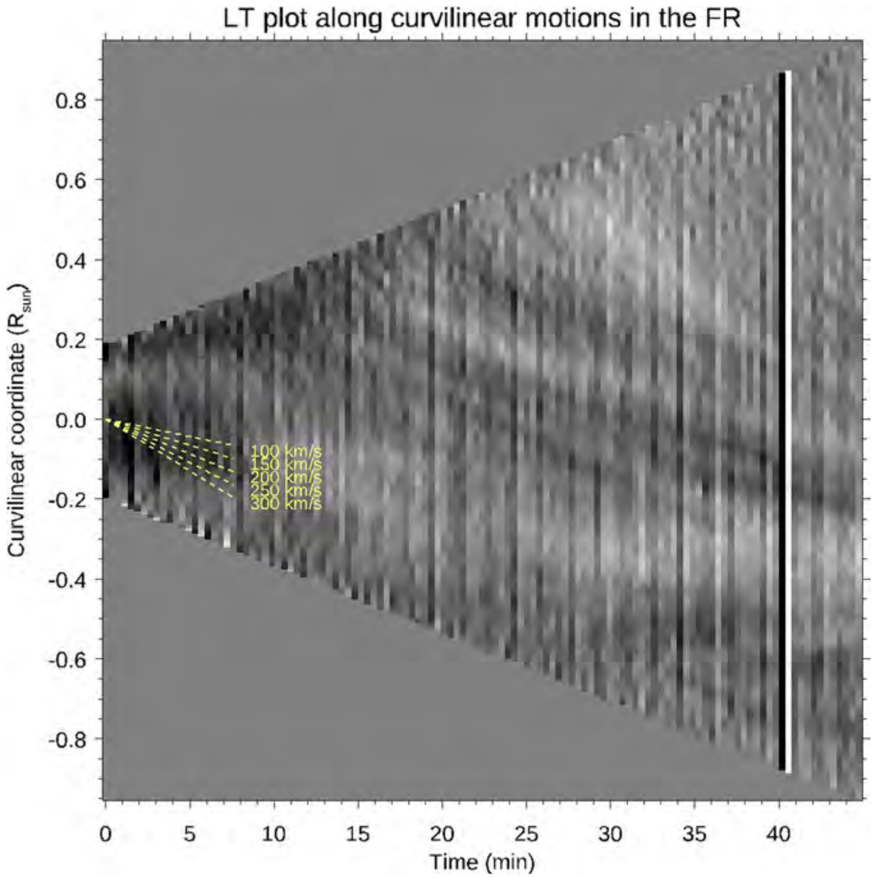

Figure 10. Map of tracks resulting by cutting semicircular intensity profiles from the running difference images moving with the expanding CME void. The dashed lines on the left show the reference inclinations of tracks for different theoretical speeds between 100 and 300 km s^{-1}. The vertical black and white columns on the right are instrumental artifacts.

with the expansion of a magnetic flux rope, then the structure must have formed during the eruption rather than before it. One possible explanation is magnetic reconnection within a preexisting sheared magnetic arcade, leading to the formation of the flux rope. Recent examples of rotations of flux ropes formed during the eruptions were simulated by C. Jiang et al. (2021) and Z. Zhou et al. (2022), who demonstrated that in this kind of eruption, the magnetic flux rope is formed by tether-cutting reconnection and that as the eruption goes on, the twist is enhanced by the conversion of writhe into twist and conservation of the total linking number or net winding. This conversion of writhe into twist is opposite of what is expected by the kink-instability model, in which the twist is accumulated before the eruption and then converted into writhe during the eruption.

A kink-unstable left-handed (right-handed) flux rope formed before the eruption, and transforming its twist into writhe, it will build up a left-handed (right-handed) writhe (via helicity conservation). This will result in a counterclockwise (clockwise) rotation of the rising flux rope (see, e.g., T. Török & B. Kliem 2005). On the other hand, if the flux rope is formed during the eruption via tether-cutting reconnection of a sheared arcade, the opposite will occur, and a left-handed (right-handed) writhe accumulated during the arcade shearing will be converted into a left-handed (right-handed) flux rope, transforming its writhe into a twist. Helical kink instability cannot produce a conversion of writhe into twist (T. Török et al. 2010). The circular motions observed by Metis were clockwise, which suggests either a twisting of a right-handed flux rope with the magnetic field pointing westward or a twisting of a left-handed flux rope with the magnetic field pointing eastward.

The PHI magnetograms show in the source region two larger-scale opposite polarities, with a smaller-scale negative polarity embedded within the larger-scale positive polarity (panel (a), Figure 11). Then, in the days before the eruption, the positive polarity apparently moved southward, shearing the field lines (panel (b), Figure 11). The EUV images acquired days before the eruption (middle right column in Figure 3) show a smaller-scale loop system oriented north–south, embedded within a larger-scale west–east loop system. These smaller loops connect the smaller-scale negative polarity with a nearby positive polarity (blue lines in panels (a) and (b) in Figure 11). Then, as described by E. R. Priest & D. W. Longcope (2017), a longitudinal shearing of these loops can form by "zipper reconnection" a flux rope with a twisted core (panel (c), Figure 11), a phase followed by a main reconnection that adds a layer of roughly uniform twist to the twisted core of the flux rope (panel (d), Figure 11). These different layers of twisted field lines are likely responsible for the nested structure of the CME void as observed by Metis (Figures 6 and 7). A similar interpretation was proposed by S. B. Shaik et al. (2024) to explain the nested rings observed by WISPR inside a CME as multiple concentric flux surfaces with different twists. The mentioned "zipper" and main magnetic reconnections would also account for the formation of the posteruption loops observed by FSI (right column in Figure 2). Then, the expansion of the flux rope formed during the eruption (panel (e), Figure 11) pushed outward the overlying larger-scale loops,

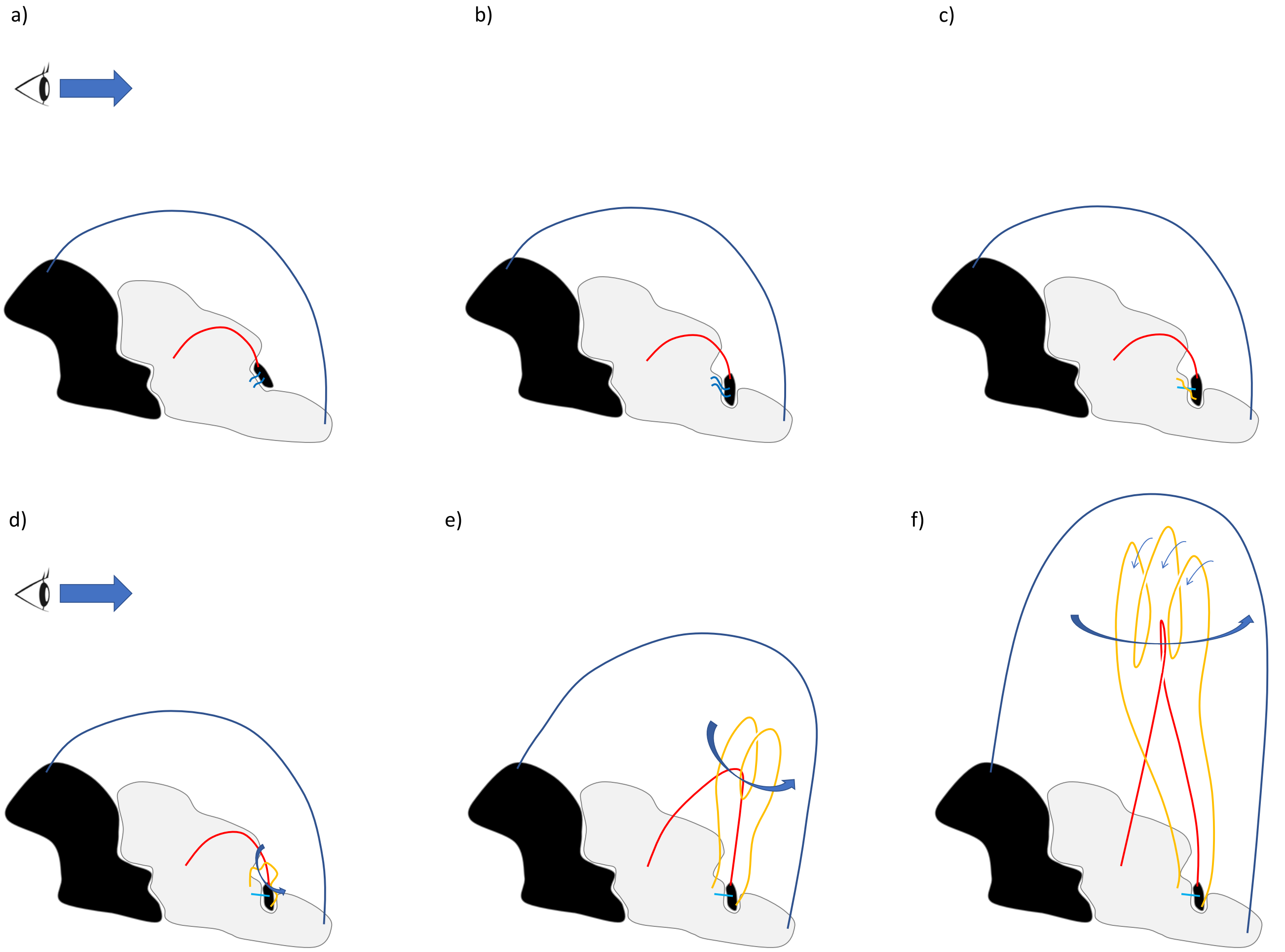

Figure 11. A cartoon showing the proposed interpretation for the eruption reported here. In detail, the bipolar CME source region showed a smaller-scale negative polarity embedded in the larger-scale positive polarity (panel (a)). The southward migration of the embedded smaller polarity caused a shearing of field lines (blue lines in panels (a) and (b)), accumulating writhe in the sheared loops. This led to the formation of a magnetic flux rope by "zipper reconnection" mostly oriented north–south (orange line, panel (c)), adding twist in the flux rope by main reconnection (panel (d)). The resulting flux-rope structure erupted, forming the CME void rotating counterclockwise (thick blue arrow, panel (d)), triggering the nearby east–west system of field lines (red line, panels (a)–(d)), leading to its expansion (panel (e)) and the formation of the CME core (panel (f)). Finally, the conversion of writhe into twist led to the clockwise motions observed by Metis inside the CME void (thin blue arrows, panel (f)). In all panels, the eye with the broad blue arrow represents the Solar Orbiter line of sight on the day of the eruption. Different colors correspond to different CME features outlined in the bottom panels of Figure 6 and in particular the CME front (dark blue), CME void (orange), and CME core (red).

leading to the formation of the CME front (panel (f), Figure 11) observed by Metis (Figure 5). During the expansion, the flux-rope counterclockwise rotation (thick blue arrows in panels (d), (e), and (f) in Figure 11) converts the writhe into twist, leading finally to the clockwise plasma motions observed by Metis inside the CME void (light blue arrows in panel (f) of Figure 11).

If, as discussed before, the eruption was triggered inside the source AR in correspondence with the smaller-scale negative polarity embedded in the larger-scale positive polarity shown by PHI magnetograms, the dominant field component appeared to be directed northwest, hence with a westward longitudinal component (see Figure 4). Hence, during the eruption, a counterclockwise rotation of the erupting flux rope resulted in the circular front observed almost face-on by FSI (Figure 2), whose expansion also pushed the overlying larger-scale loops leading to the formation of the nested structure observed by Metis (Figure 6) and of the CME front (Figure 5). In this interpretation, the observed deceleration of both the circular motion and the CME propagation speeds is in agreement with the model proposed by Z. Zhou et al. (2022), in which the twist increases only over the early phases of the eruption, reaching saturation as the available free magnetic energy is dissipated.

Before concluding, it is important to underline that the interpretation proposed here is only a possible explanation of a complex phenomenon that is completely new and never previously observed: circular motions of plasma within the void of a CME, faster than the CME itself. Overall, the observations analyzed here show the potential of high-cadence coronagraphic VL observations acquired by Metis in studying the internal structure of CMEs and understanding their origin. From this perspective, it will be very interesting to analyze the observations that will soon be acquired by the ASPIICS coronagraph (D. Galano et al. 2018) on board the ESA PROBA-3 mission (successfully launched on 2024 December 5), which, thanks to the use of flight formation technology, will observe the innermost regions of the off-limb corona at very high cadence (S. V. Shestov et al. 2021).

Acknowledgments

Solar Orbiter is a space mission of international collaboration between ESA and NASA, operated by ESA. We are grateful to the ESA SOC and MOC teams for their support. Metis was built and operated with funding from the Italian Space Agency (ASI), under contracts to the National Institute of Astrophysics (INAF) and industrial partners. Metis was built with hardware contributions from Germany (Bundesministerium für Wirtschaft und Energie through DLR), from the Czech Republic (PRODEX), and from ESA. The Metis team thanks the former PI, Ester Antonucci, for leading the development of Metis until the final delivery to ESA. The EUI instrument was built by CSL, IAS, MPS, MSSL/UCL, PMOD/WRC, ROB, LCF/IO with funding from the Belgian Federal Science Policy Office (BELSPO/PRODEX PEA 4000112292 and 4000134088); the Centre National d'Etudes Spatiales (CNES); the UK Space Agency (UKSA); the Bundesministerium für Wirtschaft und Energie (BMWi) through the Deutsches Zentrum für Luft- und Raumfahrt (DLR); and the Swiss Space Office (SSO). The German contribution to SO/PHI is funded by the BMWi through DLR and by MPG central funds. The Spanish contribution to SO/PHI is funded by AEI/MCIN/10.13039/501100011033/ and European Union "NextGenerationEU/PRTR" (RTI2018-096886-C5, PID2021-125325OB-C5, PCI2022-135009-2, PCI2022-135029-2) and ERDF "A way of making Europe"; "Center of Excellence Severo Ochoa" awards to IAA-CSIC (SEV-2017-0709, CEX2021-001131-S); and a Ramón y Cajal fellowship awarded to DOS. The French to SO/PHIcontribution is funded by CNES. F. Frassati acknowledges support from INAF grant CUP C63C23000810005 "IDEA-SW—Integrating Data and Expertise to Advance Space Weather forecasting of Catastrophic Events" and from the Project "Supporto per la realizzazione degli strumenti Metis, SWA DPU e STIX" CUP F86C18000570005. A. Bemporad, R. Biondo, S. Mancuso, and R. Susino acknowledge support by the Italian PRIN 2022, project 2022294WNB entitled "Heliospheric shocks and space weather: from multispacecraft observations to numerical modeling". Finanziato da Next Generation EU, fondo del Piano Nazionale di Ripresa e Resilienza (PNRR) Missione 4 "Istruzione e Ricerca" - Componente C2 Investimento 1.1, 'Fondo per il Programma Nazionale di Ricerca e Progetti di Rilevante Interesse Nazionale (PRIN).

ORCID iDs

Alessandro Bemporad https://orcid.org/0000-0001-5796-5653
Vincenzo Andretta https://orcid.org/0000-0003-1962-9741
Aleksandr Burtovoi https://orcid.org/0000-0002-8734-808X
Silvano Fineschi https://orcid.org/0000-0002-2789-816X
Federica Frassati https://orcid.org/0000-0001-9014-614X
Catia Grimani https://orcid.org/0000-0002-5467-6386
Federico Landini https://orcid.org/0000-0001-8244-9749
Salvatore Mancuso https://orcid.org/0000-0002-9874-2234
Giampiero Naletto https://orcid.org/0000-0003-2007-3138
Gianalfredo Nicolini https://orcid.org/0000-0002-9459-3841
Maurizio Pancrazzi https://orcid.org/0000-0002-3789-2482
Julian Blanco Rodríguez https://orcid.org/0000-0002-2055-441X
Marco Romoli https://orcid.org/0000-0001-9921-1198
Giuliana Russano https://orcid.org/0000-0002-2433-8706
Clementina Sasso https://orcid.org/0000-0002-5163-5837
Daniele Spadaro https://orcid.org/0000-0003-3517-8688
Marco Stangalini https://orcid.org/0000-0002-5365-7546
David Orozco Suárez https://orcid.org/0000-0001-8829-1938
Roberto Susino https://orcid.org/0000-0002-1017-7163
Luca Teriaca https://orcid.org/0000-0001-7298-2320
Michela Uslenghi https://orcid.org/0000-0002-7585-8605
Gherardo Valori https://orcid.org/0000-0001-7809-0067

References

Antonucci, E., Kohl, J. L., Noci, G., et al. 1997, ApJL, 490, L183
Antonucci, E., Romoli, M., Andretta, V., et al. 2020, A&A, 642, A10
Bemporad, A., Raymond, J., Poletto, G., & Romoli, M. 2007, ApJ, 655, 576
Brueckner, G. E., Howard, R. A., Koomen, M. J., et al. 1995, SoPh, 162, 357
Chen, J., Howard, R. A., Brueckner, G. E., et al. 1997, ApJL, 490, L191
Chen, P. F. 2011, LRSP, 8, 1
Ciaravella, A., Raymond, J. C., Thompson, B. J., et al. 2000, ApJ, 529, 575
Colaninno, R. C., & Vourlidas, A. 2009, ApJ, 698, 852
De Leo, Y., Burtovoi, A., Teriaca, L., et al. 2023, A&A, 676, A45
Dere, K. P., Brueckner, G. E., Howard, R. A., Michels, D. J., & Delaboudiniere, J. P. 1999, ApJ, 516, 465
Fineschi, S., Naletto, G., Romoli, M., et al. 2020, ExA, 49, 239
Forbes, T. G. 2000, JGR, 105, 23153
Galano, D., Bemporad, A., Buckley, S., et al. 2018, Proc. SPIE, 10698, 106982Y
Gallagher, P. T., Lawrence, G. R., & Dennis, B. R. 2003, ApJL, 588, L53
Gibson, S. E., & Fan, Y. 2006, JGRA, 111, A12103
González-Gómez, D. I., Blanco-Cano, X., & Raga, A. C. 2010, AdSpR, 46, 22
Howard, R. A., Moses, J. D., Vourlidas, A., et al. 2008, SSRv, 136, 67
Illing, R. M. E., & Hundhausen, A. J. 1986, JGR, 91, 10951
Jiang, C., Feng, X., Liu, R., et al. 2021, NatAs, 5, 1126
Krall, J., Chen, J., Duffin, R. T., Howard, R. A., & Thompson, B. J. 2001, ApJ, 562, 1045
Kumar, P., Cho, K. S., Bong, S. C., Park, S.-H., & Kim, Y. H. 2012, ApJ, 746, 67
Lin, J., Ko, Y. K., Sui, L., et al. 2005, ApJ, 622, 1251
Mancuso, S., & Bemporad, A. 2009, AdSpR, 44, 451
Müller, D., Nicula, B., Felix, S., et al. 2017, A&A, 606, A10
Müller, D., St. Cyr, O. C., Zouganelis, I., et al. 2020, A&A, 642, A1
Plunkett, S. P., Vourlidas, A., Šimberová, S., et al. 2000, SoPh, 194, 371
Priest, E. R., & Longcope, D. W. 2017, SoPh, 292, 25
Rochus, P., Auchère, F., Berghmans, D., et al. 2020, A&A, 642, A8
Scherrer, P. H., Schou, J., Bush, R. I., et al. 2012, SoPh, 275, 207
Shaik, S. B., Linton, M. G., Gibson, S. E., et al. 2024, ApJ, 976, 179
Shestov, S. V., Zhukov, A. N., Inhester, B., Dolla, L., & Mierla, M. 2021, A&A, 652, A4
Solanki, S. K., del Toro Iniesta, J. C., Woch, J., et al. 2020, A&A, 642, A11
Stenborg, G., & Cobelli, P. J. 2003, A&A, 398, 1185
Sterling, A. C., Moore, R. L., & Hara, H. 2012, ApJ, 761, 69
Thernisien, A. F. R., Howard, R. A., & Vourlidas, A. 2006, ApJ, 652, 763
Török, T., Berger, M. A., & Kliem, B. 2010, A&A, 516, A49
Török, T., & Kliem, B. 2005, ApJL, 630, L97
Vourlidas, A., Howard, R. A., Plunkett, S. P., et al. 2016, SSRv, 204, 83
Vourlidas, A., Lynch, B. J., Howard, R. A., & Li, Y. 2013, SoPh, 284, 179
Williams, D. R., Török, T., Démoulin, P., van Driel-Gesztelyi, L., & Kliem, B. 2005, ApJL, 628, L163
Wood, B. E., Karovska, M., Chen, J., et al. 1999, ApJ, 512, 484
Zhou, Y., Ji, H., & Zhang, Q. 2023, SoPh, 298, 35
Zhou, Z., Jiang, C., Liu, R., et al. 2022, ApJL, 927, L14